Structural investigations of Al5Co2(2-10) and (100) surfaces: Influence of bonding strength and annealing temperature on surface terminations

M. Meier, J. Ledieu, M.-C. De Weerd, V. Fournée, Emilie Gaudry

Structural investigations of $Al_5Co_2(2\bar{1}0)$ and (100) surfaces: Influence of bonding strength and annealing temperature on surface terminations

M. Meier, J. Ledieu, M.-C. De Weerd, V. Fournée,* and É. Gaudry†
Institut Jean Lamour, UMR CNRS 7198, Université de Lorraine, 54011 Nancy cedex, France
(Received 12 June 2015; revised manuscript received 13 November 2015; published 4 February 2016)

Structural investigations of the $(2\bar{1}0)$ and (100) surfaces of Al_5Co_2 using experimental ultrahigh vacuum techniques and *ab initio* computational methods are presented in this work. Both surfaces are identified and show bulk terminations where only specific atoms remain. These atoms can be seen as truncated parts of chemically bonded atomic motifs which have been identified in the bulk in a previous work [M. Meier *et al.*, Phys. Rev. B **91**, 085414 (2015)]. Whereas the $(2\bar{1}0)$ surface presents a single termination, the structure of the (100) topmost layers is found to be highly dependent on the preparation conditions, especially on the annealing temperature. This behavior, also observed for the (001) surface studied previously, can be partly explained when considering the bonding strength of the truncated motif parts with the subsurface.

DOI: 10.1103/PhysRevB.93.075412

I. INTRODUCTION

Recent advances in heterogeneous hydrogenation catalysis have identified few complex intermetallic compounds as promising candidates for the development of efficient cheap catalytic materials [1]. The performances of these catalysts have been ascribed to their specific surface structure, made of small, stable, and well-separated atomic ensembles containing generally a unique active transition metal element. This is referred as the site isolation concept [2].

The Al_5Co_2 compound is one such phase. It is an approximant to the quasicrystalline decagonal phase with the shortest periodic stacking sequence along the tenfold axis [4]. The bulk Al_5Co_2 structure, initially reported in Ref. [5], belongs to the $P6_3/mmc$ ($hP28$, 194) space group, with lattice parameters $a = b = 7.6717$ Å and $c = 7.6052$ Å [6–8]. Recently, the (001) surface of Al_5Co_2 was investigated as a first step towards the understanding of its possible catalytic properties for the semihydrogenation of acetylene [3], using both experimental and computational approaches. This previous study showed that the (001) surface terminates at specific bulk planes perpendicular to the [001] direction (pure Al planes) with a $(\sqrt{3} \times \sqrt{3})R30°$ reconstruction. The reconstruction could be ascribed to the absence of specific sets of atoms identified as parts of chemically bonded motifs present in the bulk. There are two different motifs in the bulk, either a three-dimensional cluster $(Co_1)(Al_3)_6$ or a planar motif $(Co_2)_3(Al_2)_3$ with additional "glue" atoms. These structural motifs and the strongest bonds are shown in Fig. 1 [3,9]. The $(\sqrt{3} \times \sqrt{3})R30°$ reconstruction on the (001) surface is obtained by removing 2/3 of the surface Al_3 groups belonging to the three-dimensional $(Co_1)(Al_3)_6$ clusters.

Because this (001) surface termination contains no Co atoms, the chemical reactivity of the $Al_5Co_2(001)$ surface is expected to be low, although the subsurface Co atoms slightly influence the (001) surface electronic structure. In this paper, we analyze two other low-index surfaces of the same compound, namely the $(2\bar{1}0)$ and (100) surfaces. Perpendicular to the [100] direction [$(2\bar{1}0)$ atomic planes], the Al_5Co_2 crystal structure can be described as a stacking of two different layers: a dense puckered layer (P) made of twelve Al and four Co atoms and a flat layer (F) made of eight Al and four Co atoms (Fig. 1). On the contrary, no layered structure exists parallel to the [010] direction. The aim here is to describe in details the $(2\bar{1}0)$ and (100) surfaces and discuss the impact of the chemically bonded motifs on their surface structures.

The $(2\bar{1}0)$ surface structure has been investigated some years ago by first-principles calculations [10]. The influence of the atomic density and the chemical composition on the relative surface stability of the two possible bulk terminations F or P were investigated. The results showed that the dense Al-rich P layers have a lower surface energy compared to F layers. However, these results could not be compared to any experimental observations at that time. In the present paper, experimental and theoretical approaches are combined to describe in details the surface structures and identify the physical parameters at the origin of the observed surface structures.

We use an experimental approach where single crystal surfaces are investigated under ultra-high vacuum (UHV) by x-ray photoelectron spectroscopy (XPS), low-energy electron diffraction (LEED) and scanning tunneling microscopy (STM) combined with a first-principles study based on density functional theory (DFT). Section II presents the main experimental and computational details. Section III is divided into two subsections, dedicated to either the $(2\bar{1}0)$ or (100) surface. For each surface, both experimental and calculated results are presented and discussed in order to determine the most stable surface model. The influence of the annealing temperature is also investigated. Results are then discussed in Sec. IV before we conclude in Sec. V.

II. METHODS

In this work, we use a combination of (i) an experimental approach based on surface science techniques and (ii) a theoretical approach based on density functional theory calculations. To identify the observed surface structures, we consider structural models which are all built based on bulk truncations

*vincent.fournee@univ-lorraine.fr
†emilie.gaudry@univ-lorraine.fr

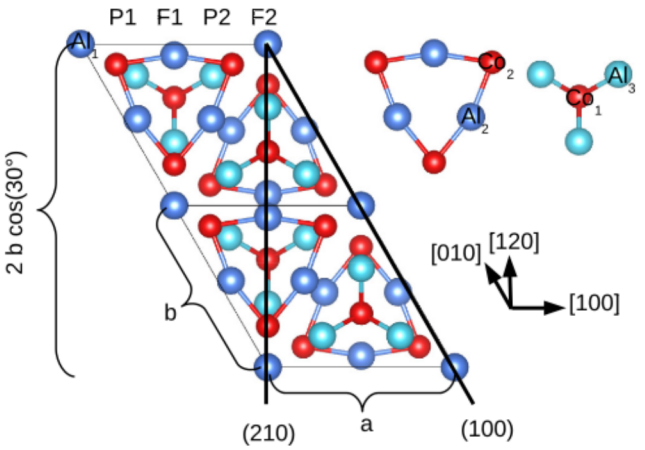

FIG. 1. (Left) Layer stacking perpendicular to the [100] direction [blue (red) spheres are Al (Co) atoms]. The strongest chemical bonds are represented by lines connecting atoms. The $(2\bar{1}0)$ plane is forming a 30° angle with $\vec{b}$. A $2 \times b\cos(30°)$ distance is needed to describe the complete structure in the [120] direction. $Al_{1,2,3}$ and $Co_{1,2}$ refer to the five nonequivalent atomic positions. (Right) Chemically bonded motifs present in the bulk: planar motif $(Co_2)_3(Al_2)_3$ and 3D motif $(Co_1)(Al_3)_6$ viewed from the top.

such as to reproduce the experimental observations as much as possible. We have not considered more sophisticated models which could be obtained by changing the chemical nature of the elements or by introducing new atomic positions, considering that the agreement between our models and the experiments is already fair, although there is always space for improvement.

A. Experimental details

Details on crystal growth can be found in Meier *et al.* [3]. For surface investigations, two samples were extracted from the ingot exposing either a $(2\bar{1}0)$ or a (100) surface (see Fig. 1). The same ingot was already used in the study of the (001) surface presented in our recent work [3]. The samples were oriented using back scattered x-ray Laue diffraction within 0.5°, polished down to 0.25 μm using diamond paste and mounted on a Ta plate. Once inserted in the UHV chamber, clean surfaces were achieved by cycles of sputtering (Ar^+, 1.5 kV, 30 min) and annealing at 973 K for 1 hour if not specified otherwise. An optical pyrometer with an emissivity set to 0.35 was used to measure the temperature. The surface composition and cleanliness were monitored by XPS using a nonmonochromated Mg Kα x-ray source. LEED and STM measurements gave access to the surface structure, while the surface electronic structure was probed by room-temperature ultraviolet photoelectron spectroscopy (UPS, He I, 21.2 eV).

B. Calculation details

DFT calculations using the plane wave Vienna *ab initio* simulation package (VASP) [11–14] were performed to complement our experimental study. The interaction between the valence electrons and the ionic core is described using the projector-augmented wave (PAW) method [15,16] and the calculations are performed within the generalized gradient approximation (GGA-PBE) [17,18]. Atomic structures were plotted using VESTA [19].

Total energy calculations on the bulk model were performed using a cutoff energy (E_{cut}) and a number of k points within the Brillouin zone such as to achieve an energy precision lower than 0.06 meV/at. ($E_{\text{cut}} = 450$ eV and k-point grid set to $8 \times 8 \times 8$). The k-point grids were adjusted for the $(2\bar{1}0)$ surface to $1 \times 4 \times 8$ and for the (100) surface to $1 \times 8 \times 8$.

The different surface models were built using asymmetric slabs with $\simeq$64% of the slab being fixed. Neighboring images of the slab were separated by a 11-Å-thick vacuum layer. For the $(2\bar{1}0)$ surface, it corresponds to a seven-layer-thick fixed part and an additional four- or five-layer-thick relaxed part on top (F or P layer termination).

These slab parameters were optimized to guarantee that (i) the forces on the last fixed layer are minimized, (ii) the distance between the last fixed layer and the first relaxed layer (d) is close to the bulk interlayer distance (d_0). For the $(2\bar{1}0)$ surface, $\frac{|d-d_0|}{d} = 0.01\%$ (the exact value depends on the considered model; here this value is for the P_B model, see Sec. III A 2) and 0.04% for the (100) surface (A^{+1} model, see Sec. III B 2). This later value was obtained by considering the average relaxation of specific atoms slightly above the fixed/relaxed limit, since there are no well-defined layers in this case. The forces acting on the atoms of the last fixed layer were approximately 0.06 and 0.08 eV/Å for average in-plane forces ($\|$) and 0.03 and 0.08 eV/Å for average normal forces ($\perp$), for $(2\bar{1}0)$ P_B model, and (100) A^{+1} model, respectively. For the relaxed part of the slab, the convergence condition consists of forces acting on the relaxed atoms smaller than 0.02 eV/Å.

The parameters used in the present study correspond to the largest slab we could reasonably use for the calculations. The number of atoms for the $(2\bar{1}0)$ surface models already exceeds 300 atoms. Nevertheless, the considered slab size leads to reasonable results: the difference in the surface energy of two slabs built with m atomic layers and n void layers is about 0.01 J m^{-2} for $(m, n) = (6, 5), (6, 9), (12, 5)$, or $(12, 9)$ (P_B model).

Surface energies were calculated using the method described in Ref. [3], and plotted as a function of the Al chemical potential. The allowed range of the Al chemical potential was determined in our previous study [3] by two different methods, giving similar results $[(\mu_{\text{Al}} - \mu_{\text{Al}}^{\text{bulk}}) \in [-0.65; 0]$ eV or $[-0.60; -0.03]$ eV].

For the $(2\bar{1}0)$ surface, the surface electronic structures were calculated for the different models using simplified slabs (from $\sim$300 atoms down to $\sim$150 atoms). For one of the models (P_B, see Sec. III A 2), the electronic structure was also calculated using a larger slab containing 328 atoms for comparison purposes. The number of k points was multiplied by two for DOS calculation. Overall, the total DOS were found similar for the two types of slabs, except for a slight increase of the number of states at the Fermi energy observed for the simplified slab. It has already been shown [20] that a too small slab thickness can produce a change in the number of states at the Fermi energy, in agreement with our finding. However, the projected DOS for the S layer shown in Fig. 2 (left) is nearly identical for the two slab thicknesses. DOS calculations were done without any spin polarization since the considered surface does not show any magnetic moment. As an illustration, Fig. 2 (right) shows the projected DOS (spin considered) for the surface layer, with

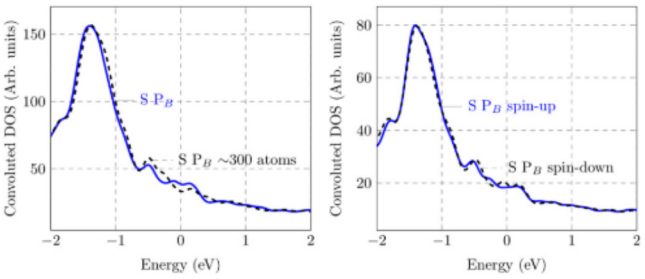

FIG. 2. (Left) Calculated projected surface (S) layer DOS for the $(2\bar{1}0)$ surface (P_B model) for the simplified slab containing 160 atoms (plain blue line) and for the nonsimplified slab (dashed black line). Here, the spin is not considered. (Right) Calculated projected S layer DOS for the $(2\bar{1}0)$ surface (P_B model) with spin-up (plain blue line) and spin-down (dashed black line) contributions.

nearly identical spin-up and spin-down contributions (for the P_B model). This validates our choice of using simplified slabs and no spin polarization for the DOS calculations.

III. RESULTS

A. The $(2\bar{1}0)$ surface

1. Experimental results

The chemical composition of the $(2\bar{1}0)$ surface has been investigated by XPS as a function of the photoelectron take-off angle. Similar to the study of the (001) surface [3], the results show an almost constant concentration with varying surface sensitivity. We can conclude that no significant segregation occurs for the $(2\bar{1}0)$ surface.

Figure 3 shows a LEED pattern of the $(2\bar{1}0)$ surface prepared at 973 K. The momentum space is calibrated using a reference LEED pattern recorded on a Al(111) surface under identical conditions. The periodicity along the [120] direction is measured at 26.1 ± 0.4 Å [$\sim 2 \times 2b\cos(30°)$] and 7.4 ± 0.4 Å along the [001] direction ($\sim c$). These diffraction

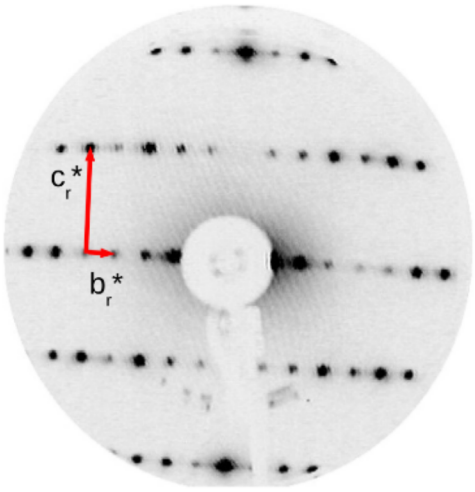

FIG. 3. LEED pattern at 20 eV of the $Al_5Co_2(2\bar{1}0)$ surface prepared at 973 K showing a (2×1) reconstruction.

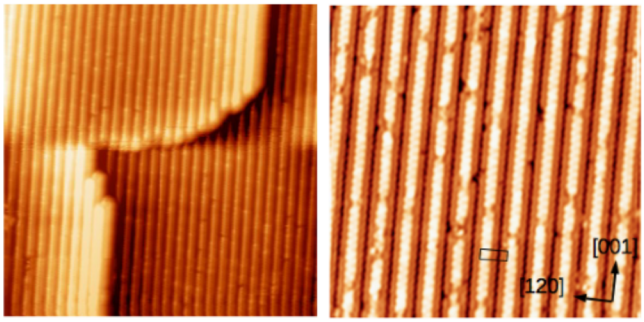

(a) (b)

FIG. 4. (a) 75×75 nm^2 STM image of the $Al_5Co_2(2\bar{1}0)$ surface prepared at 973 K ($V_b = -2$ V; $I_t = 0.1$ nA) and (b) 20×20 nm^2 ($V_b = -1$ V; $I_t = 0.2$ nA). The unit cell of the reconstruction is also shown.

patterns indicate a doubling of the periodicity along [120] (Fig. 1) and thus a (2×1) surface reconstruction.

STM images show the existence of terraces separated by a unique step height of 3.8 ± 0.2 Å, which is equal to $\sim a/2$ [Fig. 4(a)]. This indicates that only P- or F-type layers appear as surface termination.

At higher resolution, Fig. 4(b) shows approximately 12.0 ± 0.2 Å wide lines running along the [001] direction. The distance between two consecutive lines is 26.3 ± 0.2 Å [$\sim 2 \times 2b\cos(30°)$]. In the [001] direction, a periodicity of 7.4 ± 0.2 Å is measured, which corresponds to $\sim c$. This is in agreement with the LEED measurements and confirms the (2×1) reconstruction. The line profiles along the [120] direction indicate a peak-to-peak roughness of 2.4 ± 0.2 Å corresponding to the height difference between F layer and protruding atoms of the P layer, which is ~2.3 Å.

2. Theoretical results

Using the knowledge gained from these experimental observations, we could create different surface models starting from the bulk structure. While both types of layers (P and F) have been considered here, it was not possible to create a model based on the F layer which could geometrically match the observed (2×1) reconstruction. Figure 5 shows the complete P layer and seven different models consisting of an incomplete P layer that could match the experimental observations.

The complete P layer model can be seen as a succession of two different zigzagging lines of Co atoms extending along c. The first one has Al pentagons capped by Co atoms (called T line) and the second one consists of Al pentagons located on top of Co atoms (called B line) [Fig. 5(a)].

To obtain the (2×1) reconstruction, different atoms or groups of atoms can be removed. A first possibility [Fig. 5(b)] is to remove the Al pentagons every two B lines and to keep the T lines unchanged. The resulting model is referred as P_A model. The second model is called P_{A-4Co} [Fig. 5(c)]. It is similar to the first one but the four Co atoms on the T lines (on top of the Al pentagons) are also removed. The P_B model [Fig. 5(d)] is obtained by removing all atoms on every second B line. Here again, a P_{B-4Co} model [Fig. 5(e)] can be created by also removing the four Co atoms on the T lines. For the

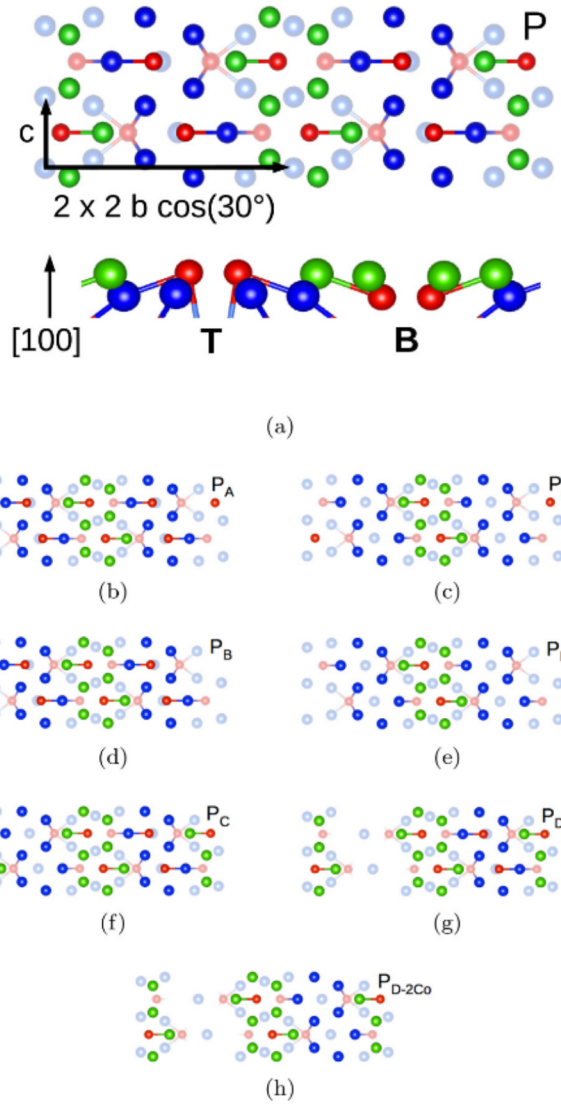

FIG. 5. (a) Top and side view of the complete P termination. The T and B lines are shown. Blue and green spheres are Al atoms, red spheres are Co atoms. The magnitudes of the basis vectors of the reconstructed unit cell are c and $4b\cos(30°)$. (b) P_A model generated by removing the Al pentagons every two B lines, while keeping the T lines unchanged, (c) P_{A-4Co}, (d) P_B obtained by removing all atoms on every second B line, (e) P_{B-4Co}, (f) P_C formed by removing the Co atoms of every second T line, (g) P_D obtained by removing all of its atoms on every second T line and (h) P_{D-2Co}.

P_C model [Fig. 5(f)], the Co atoms of every second T line are removed. The P_D model [Fig. 5(g)] has all of its atoms on every second T line removed. For P_{D-2Co} model [Fig. 5(h)], two additional Co atoms on the remaining T lines are also removed.

The surface energies of the different models have been calculated and are presented in Fig. 6. Surface energies of nonreconstructed terminations (P- and F-type) are in agreement with those calculated in Ref. [10]. P_B and P_{B-4Co} models show the lowest surface energy for $\mu_{Al} - \mu_{Al}^{bulk} < -0.35$ eV and $\mu_{Al} - \mu_{Al}^{bulk} > -0.35$ eV, respectively.

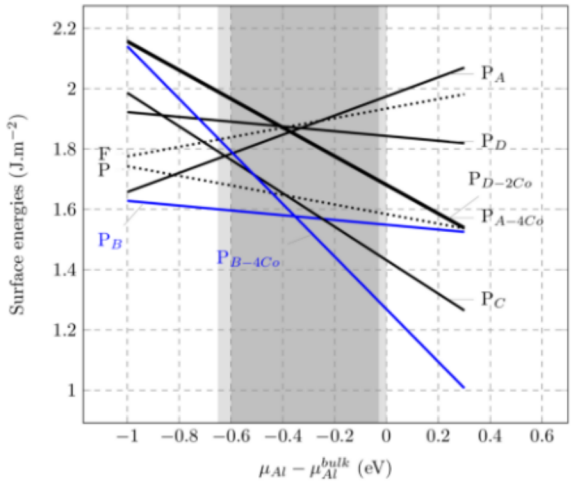

FIG. 6. Calculated surface energies for all seven models (continuous lines) matching the experimental LEED and STM results and non reconstructed terminations P and F (dashed lines), plotted as a function of $\mu_{Al} - \mu_{Al}^{bulk}$.

STM images have been simulated within the Tersoff-Hamann approximation [21,22] for the two models P_B and P_{B-4Co} (Fig. 7). A small bias dependency can be observed on the experimental images between positive and negative biases. The lines seem overall straighter for negatives biases. This is qualitatively well reproduced for both models. A zigzagging line with a dimmer contrast can be seen in the center of the 12-Å-wide lines on simulated images at positive biases, which can hardly be seen in the experimental images.

A comparison of the DOS obtained for P_B and P_{B-4Co} models, using the simplified slabs mentioned earlier, is presented in Fig. 8. The projected DOS for the surface layer and subsurface layers (down to $S-2$) are compared with the equivalent bulk layers (called Eq-S to Eq-$S-2$). The surface layer projected DOS shows that the pseudogap is being filled at the surface for both models. The pseudogap, characteristic of Hume-Rothery compounds and resulting from the interaction between the Fermi surface and a predominant Brillouin zone and $sp-d$ hybridization, disappears for the S layer. An increase in the number of states at the Fermi energy has already been observed for the (001) surface models [3] (the

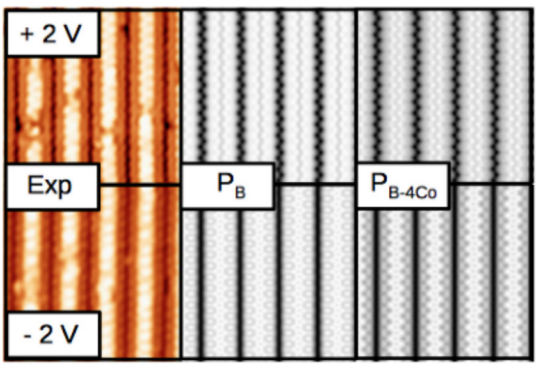

FIG. 7. Experimental STM images, P_B and P_{B-4Co} simulated STM images (at $V_b = \pm 2$ V).

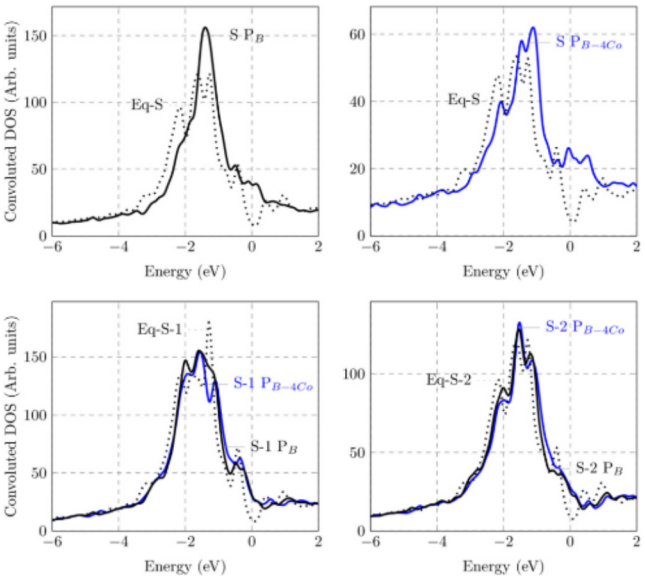

FIG. 8. Calculated DOS for the P_B model and for the P_{B-4Co} model, projected on surface (S) and subsurface planes (S − 1) to (S − 2) (thick lines). The dotted lines show the bulk DOS of corresponding bulk planes.

surface showed only 1/3 of the bulk pseudogap). Here, this phenomenon is amplified, although a part of this increase could be ascribed to the too thin slab used, an artifact mentioned previously. The overall narrower *d*-band seen for S and even S − 1 projected DOS resulting from a lower coordination number for surface atoms, is leading to an up-shift of the *d*-band center closer to the Fermi energy [23].

3. Combining experimental and theoretical results

The experimental study demonstrates that the surface consists in a single termination and that no sizable segregation occurs. A (2 × 1) surface reconstruction is observed by LEED and STM with 12-Å-wide lines running parallel to the *c* axis. Surface energy calculations show that among the models considered here, two models matching the experimental geometry should be considered: the P_{B-4Co} model for the Al-rich part of the chemical potential ($\mu_{Al} - \mu_{Al}^{bulk} > -0.35$ eV) and the P_B model for the Co-rich part ($\mu_{Al} - \mu_{Al}^{bulk} < -0.35$ eV). These two models are based on the same surface termination but differ by the presence (or absence) of four Co surface atoms. As seen in Fig. 7, the small bias dependency observed experimentally is also reproduced in simulated STM images of both models. However, a comparison between experimental and simulated images does not allow us to discriminate between the two models.

In addition, UPS measurements have been carried out on the surface. Figure 9 shows the experimental valence band which is compared to the calculated surface (S) and subsurface (S − 1) layers DOS of the P_B and P_{B-4Co} models. A qualitative agreement is obtained, all major peaks are reproduced for both models (main peak at −1.25 eV and shoulder at −0.5 eV). This gives further support to the proposed surface models.

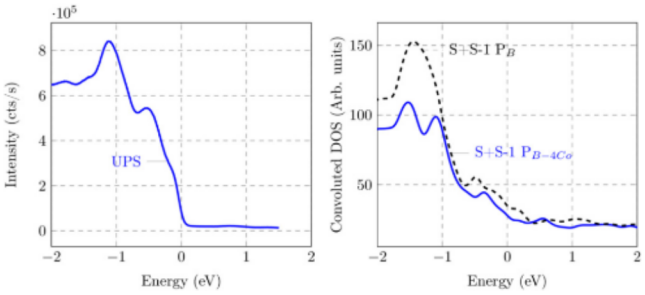

FIG. 9. UPS data and calculated projected DOS for surface (S) and subsurface (S − 1) layers for P_B (dashed black line) and P_{B-4Co} (blue line) models.

4. Other structures of the $(2\bar{1}0)$ surface

The surface has also been prepared at 2 other annealing temperatures (823 and 1043 K) and additional structures have been observed as described below.

(a) Low-temperature phase (823 K). Additional spots appear on the LEED pattern for the surface prepared at 823 K [Fig. 10(a)]. These spots correspond to 2 oblique unit mesh domains rotated by 120° from each other and having lattice parameters $x = 2.7 \pm 0.4$ Å and $y = 4.5 \pm 0.4$ Å. The reciprocal lattices of the two oblique domains are not commensurate with the (2 × 1) pattern. The *y* axis of the two domains are rotated by ± 60° with respect to the substrate *c*

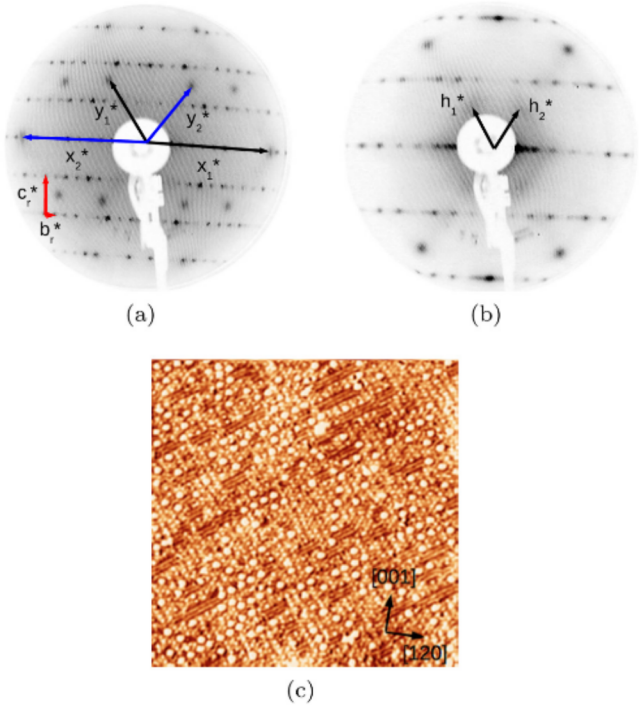

FIG. 10. (a) LEED pattern at 60 eV of the $Al_5Co_2(2\bar{1}0)$ surface prepared at 823 K with *x* and *y* oblique unit mesh domains (orientated at ± 60° with respect to the *c* axis) parameters. (b) LEED pattern at 20 eV of the $Al_5Co_2(2\bar{1}0)$ surface prepared at 823 K, showing a diffuse hexagonal unit cell (h_1 and h_2). (c) 30 × 30 nm² STM image ($V_b = -1$ V; $I_t = 0.1$ nA) showing one domain.

axis. At lower energy [Fig. 10(b)], the LEED pattern shows a very diffuse hexagonal unit mesh with lattice parameter equal to 11.5 ± 0.4 Å. The diffraction spots obtained for the surface prepared at 973 K corresponding to a (2×1) reconstruction are also already present.

The (2×1) reconstruction described previously when annealing the sample to 973 K is also observed at this temperature. In addition, parts of the surface area exhibit a new phase as observed by STM [see Fig. 10(c)]. This phase shows atomic rows oriented at $-60°$ with respect to the substrate c axis. The distance between the rows corresponds to $y \sin(60°)$. The poor resolution of the STM image could not allow to measure x. Among the different features observed, the largest protrusions form an hexagonal unit mesh, which is in agreement with the LEED pattern obtained at lower energy mentioned previously. The distance between two protrusions is 11 ± 0.2 Å. The second domain (oriented at $+60°$ with respect to the [001] axis) could also be observed. The step height between consecutive terraces is 1.9 Å corresponding to the distance between F and P layers.

Note that preferential sputtering of Al occurs in this system. Near-surface concentration measurements by XPS indicate that the annealing temperature and time needed to obtain the (2×1) reconstructed surface were not achieved yet. As a consequence, the surface annealed at 823 K consisted of a mixture of the (2×1) phase and the metastable oblique domains. No simulations of this metastable phase were performed. Moreover, no monoclinic structure with such unit cell parameters exists in the Al-Co phase diagram [24], indicating that the observed phase is probably a metastable surface alloy.

(b) High-temperature phase (1043 K). The LEED pattern recorded for the surface prepared at 1043 K [Fig. 11(a)] is nearly identical to the one obtained at 973 K except for some spots, which move along b_r^* with increasing energy, indicating the formation of facets at the surface. Height histograms of STM images spanning two different terraces revealed step heights of 3.8 Å or multiples of this height. For some STM images like the one shown in Fig. 11(b), terraces of the (2×1) reconstruction appear separated by microfacets inclined by 9° to the $(2\bar{1}0)$ surface. The facets also have a row structure. The lines extending along the [001] direction are on average longer than previously observed after annealing at 973 K but the main structure [12-Å-wide lines of the (2×1) reconstruction] remains the same.

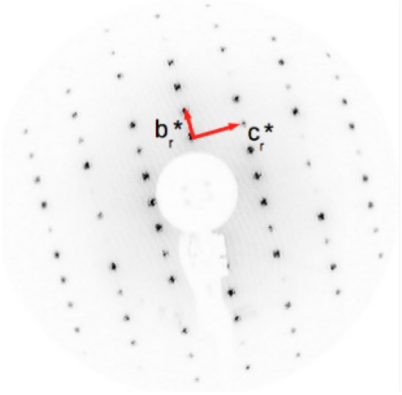

FIG. 12. LEED pattern at 55 eV of the $Al_5Co_2(100)$ surface prepared at 973 K showing a (2×1) reconstruction.

B. The (100) surface

1. Experimental results

The chemical composition of the (100) surface has been investigated by XPS as a function of the photoelectron take-off angle and revealed that no significant segregation occurs either.

Figure 12 shows the LEED pattern of the (100) surface prepared at 973 K with $b_r = 14.8 \pm 0.4$ Å and $c_r = 7.2 \pm 0.4$ Å. These diffraction spots are consistent with a (2×1) surface reconstruction.

STM images show the existence of terraces with step heights of 6.6 ± 0.2 Å, which is equal to $\sim a \cos(30°)$, normal to the (100) surface [Fig. 13(a)]. Therefore all terraces are identical and correspond to an unique termination. Figure 13(b) shows lines running along the [001] direction. Only a weak bias dependency is observed. The distance between two lines is 15.0 ± 0.2 Å. In the [001] direction, the periodicity measured on a same line is 7.4 ± 0.2 Å. This is in agreement with the LEED measurements and confirms the (2×1) reconstruction. Corrugation along the [010] direction is equal to 0.9 Å.

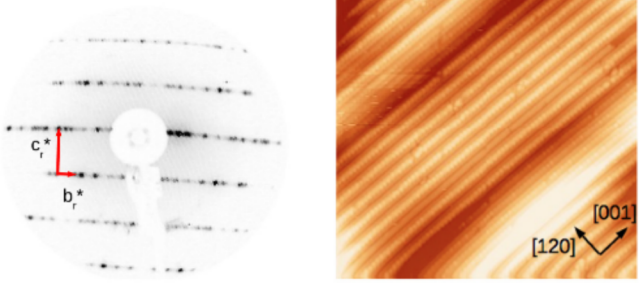

(a) (b)

FIG. 11. (a) LEED pattern at 40 eV of the $Al_5Co_2(2\bar{1}0)$ surface prepared at 1043 K, (b) 50×50 nm^2 STM image ($V_b = -2$ V; $I_t = 0.08$ nA, 45° rotated).

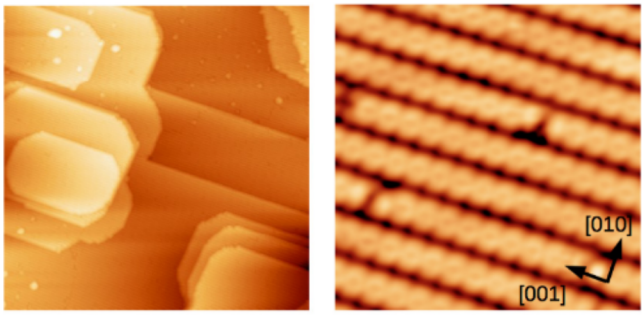

(a) (b)

FIG. 13. STM images of $Al_5Co_2(100)$ surface prepared at 973 K: (a) 150×150 nm^2 ($V_b = -2$ V; $I_t = 0.2$ nA) and (b) 10×10 nm^2 ($V_b = -1$ V; $I_t = 0.2$ nA).

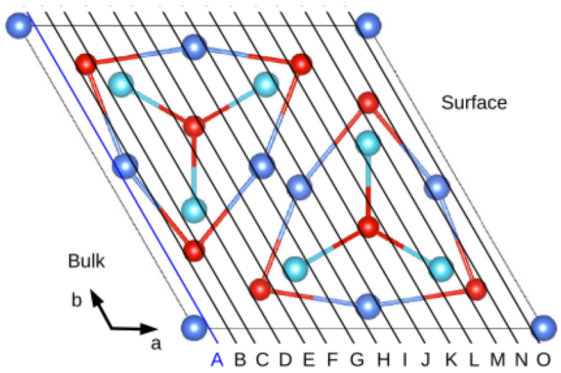

FIG. 14. Side view of all non reconstructed terminations and corresponding labels.

2. Theoretical results

In order to find the energetically most favorable surface, we have built a large number of models able to reproduce the experimental data. As there are no well-defined layers perpendicular to (100) planes, different (100) terminations labeled by letters (as shown in Fig. 14) were considered. Specific atoms were removed in order to build the (2×1) reconstruction. These (2×1) models are identified by the number of atoms missing, based on the complete termination from which it is built. The result is a total of 16 models matching geometrically the experimental reconstruction.

The surface energies of all 16 (2×1) reconstructed models considered in this study are calculated and plotted in Fig. 15. Among them, three models called A^{-2}, A^{-1}, and A^{+1} have the lowest surface energy within the allowed range of the chemical potential and for this reason they are the only models detailed here [Figs. 16(b)–16(d)]. The three models are based on the same complete termination A but differ by the number of atoms which have been removed or added to obtain the reconstruction. (A^{+1} is seen here as the complete A layer, with one additional atom. It can also be seen as a reconstruction on the adjacent layer to A, here called B, where some atoms have been removed, i.e., $A^{+1} = B^{-1}$.)

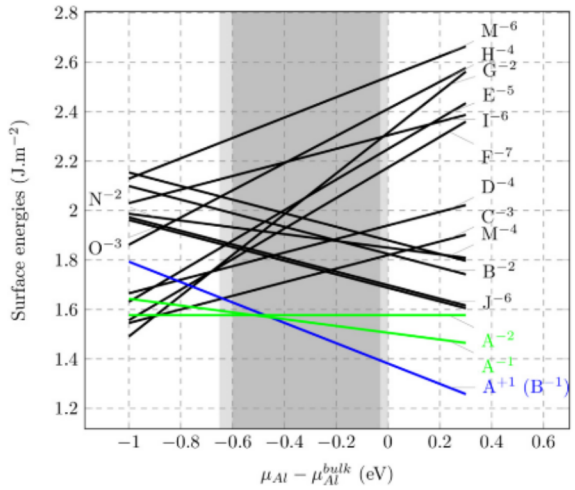

FIG. 15. Calculated surface energies for all (2×1) reconstructed models, plotted as a function of $\mu_{Al} - \mu_{Al}^{bulk}$.

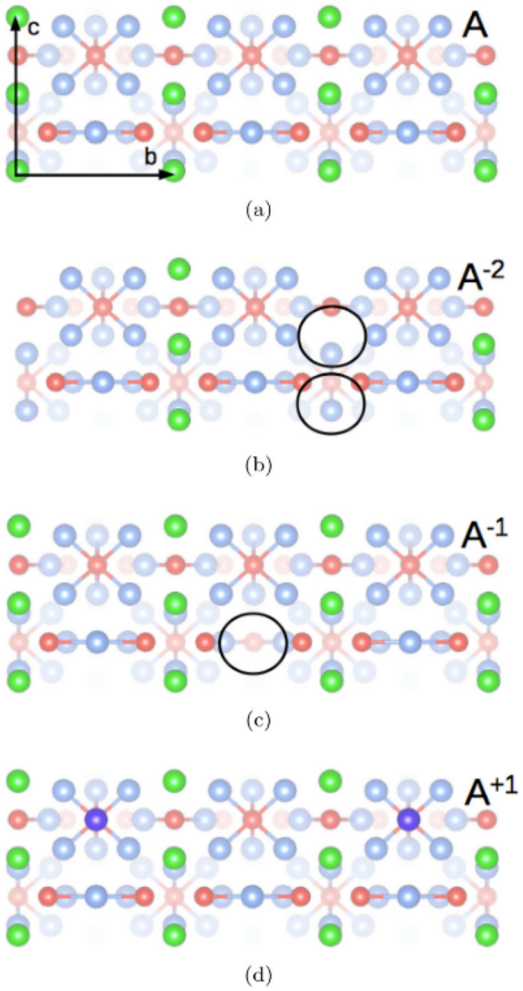

FIG. 16. (a) Complete A termination with Al atoms in green and blue, Co atoms in red, (b) A^{-2}, (c) A^{-1}, (d) A^{+1}, the circles correspond to missing atoms (compared to the complete A termination).

STM images have been simulated for A^{-2}, A^{-1}, and A^{+1} models at different bias voltages (Fig. 17). Atomic rows similar to those observed experimentally are reproduced for the three

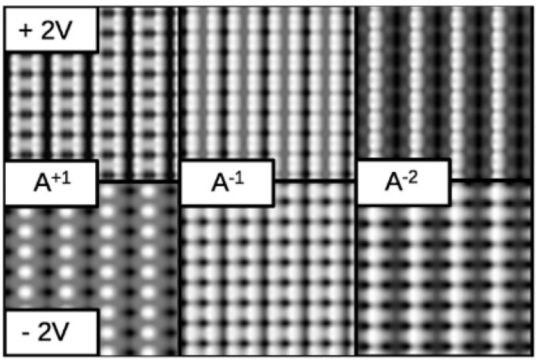

FIG. 17. A^{+1}, A^{-1}, and A^{-2} simulated STM images (at $V_b = \pm 2$ V).

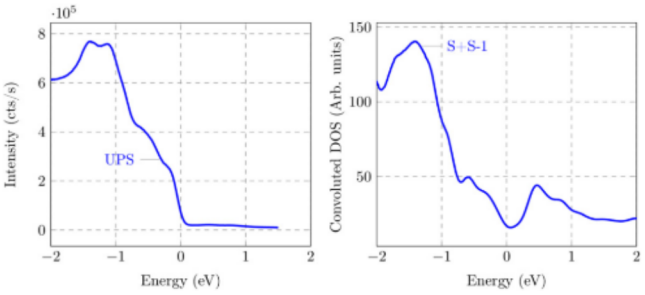

FIG. 18. UPS data and calculated DOS for surface (S) and subsurface (S − 1) layers (A^{+1}).

different models. However, the A^{-1} model shows a weaker bias dependency of the STM contrast compared to A^{-2} and A^{+1} models and agrees better with experimental images.

Finally, the valence band UPS spectrum has been recorded and compared to the projected DOS of the surface (S) and subsurface (S − 1) layers for one possible model (A^{+1}) (Fig. 18). A good agreement is found regarding the position of the main peaks below the Fermi level. The drop in the spectral intensity at E_F is consistent with the deep pseudogap in the calculated DOS.

3. Combining experimental and theoretical results

Experimental data shows a (2 × 1) surface reconstruction with lines parallel to the [001] direction. Among all considered models, three models possessing the lowest surface energies have been considered, i.e., A^{-2} and A^{-1} for the Co-rich part $[(\mu_{Al} - \mu_{Al}^{bulk}) \in [-0.6; -0.5]$ eV] and A^{+1} for the Al-rich part $[(\mu_{Al} - \mu_{Al}^{bulk}) \in [-0.5; 0]$ eV]. To eliminate further models among the three remaining ones, simulated STM images have been calculated. Model A^{-1} is favored as it shows the smallest bias dependency and better agrees with the experimental observations.

In contrast, model A^{+1} has the lowest surface energy for most values of μ_{Al}. Crystal growth conditions imply that the bulk composition should be on the Al-rich side of the existence domain of the compound, which would tend to values of μ_{Al} close to μ_{Al}^{bulk} and therefore favor model A^{+1}. In the case of the (001) surface [3], the observed termination could be interpreted using a model that was also predicted as the most stable in a narrow Al-rich μ_{Al} range, thus in agreement with our crystal growth information. This discrepancy may be due to the influence of the details in the surface preparation.

4. Other structures of the (100) surface

The surface has also been prepared at two other annealing temperatures (823 and 1043 K) and additional structures have been observed as described below.

(a) Low-temperature phase (823 K). Figure 19(a) shows the LEED pattern of the (100) surface prepared at 823 K. Additional diffuse intensity is observed in-between the spots of the (2 × 1) reconstruction, both along the b^* and c^* directions, indicative of some disorder. Figure 19(b) shows an STM image with bright atomic lines spaced by 15 Å (∼2 × b), 22.5 Å (∼3 × b), or 30 Å (∼4 × b) corresponding to patches of

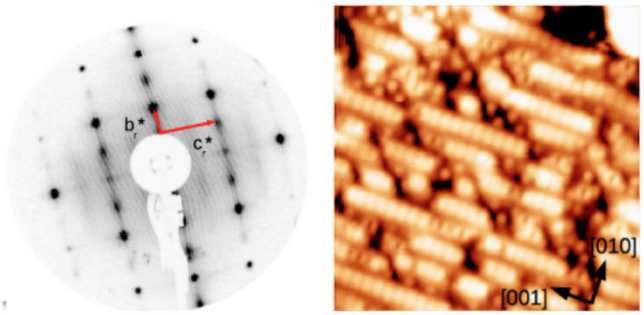

FIG. 19. (a) LEED pattern at 25 eV of the $Al_5Co_2(100)$ surface prepared at 823 K showing diffused spots along b_r^*, corresponding to a mixture of different reconstructions, (2 × 1), (3 × 1), and (4 × 1), (b) 20 × 20 nm^2 STM image of the same surface ($V_b = -2$ V; $I_t =$ 0.1 nA).

three different surface reconstructions identified; i.e., (2 × 1), (3 × 1), and (4 × 1).

The diffuse lines or streaks observed along b_r^* originate from the disorder among the line spacing in the [010] direction. Additional bright dots are observed in STM images in-between the bright lines. The dots are either aligned for the 22.5 Å spacing or forming a zigzagging chain in the case of the 30 Å spacing. Using the above information, models of the (3 × 1) and (4 × 1) reconstructions based on the A termination have been created. To take into consideration the linear or zigzagging dots observed in-between the bright lines, the (3 × 1) and (4 × 1) models have been created by adding atoms at adequate positions as observed by STM. It results in models (see Fig. 20) referred as (3 × 1)+ and (4 × 1)+. STM images have been simulated and are shown in Fig. 21(a). The (3 × 1)+ and (4 × 1)+ models reproduce well the observed dotted lines or zigzagging chains in-between the bright lines.

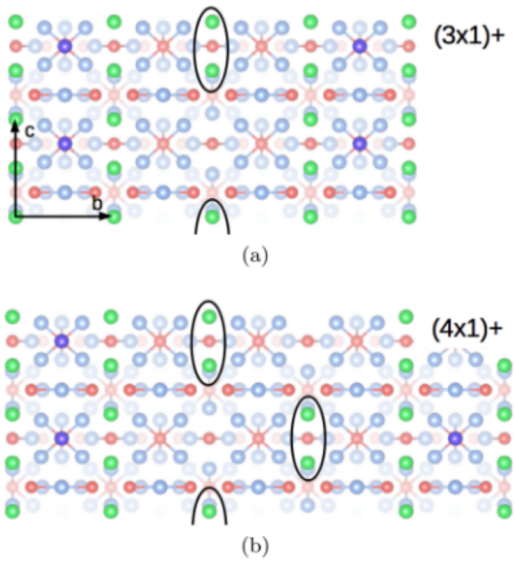

FIG. 20. Structure of the (a) (3 × 1)+ and (b) (4 × 1)+ models, + referring to models where additional atoms (in ovals) remain in the line in-between space.

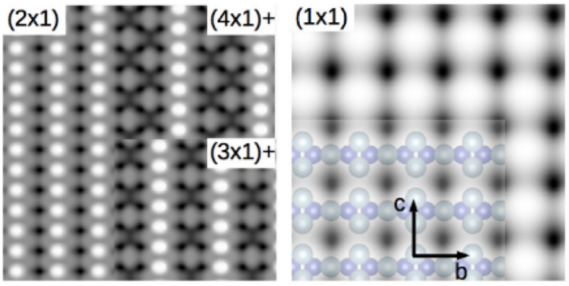

FIG. 21. (a) Simulated STM images ($V_b = -2$ V) for the A^{+1} (2×1) model (left) and (3×1)+, (4×1)+ models (right) corresponding to the experimentally observed surface prepared at lower temperature (823 K), (b) simulated STM image for the A model corresponding to the experimentally observed surface at higher preparation temperature (1043 K).

(b) High-temperature phase (1043 K). Figure 22(a) shows the LEED pattern of the (100) surface prepared at 1043 K. The observed surface is not reconstructed anymore and corresponds to a (1×1) pattern. The surface no longer shows the previously observed bright atomic rows but a pseudosquare structure [Fig. 22(b)]. The simulated STM image of the model A shown in Fig. 21(b) reproduces well the square grid of bright protrusions observed experimentally. The structure model A has been superimposed onto the calculated STM image. It can be seen that each bright dot of the square grid STM actually arises from two protruding Al atoms lying on top of a pair of subsurface Co atoms.

The surface energies have been calculated for the low- and high-temperature models (Fig. 23). It can be seen that models (3×1)+ and (4×1)+ have slightly lower surface energies than their equivalent models without the in-between line schemes [(3×1) and (4×1)] but larger surface energies than the (2×1) model (for the Al-rich part). These results suggest that the (3×1) and (4×1) reconstruction patches are metastable with respect to the (2×1) reconstruction. In addition, all A-based reconstructions have higher surface energies than the complete A termination observed at higher annealing temperatures indicating that all reconstructed surfaces are metastable phases with respect to the (1×1) termination.

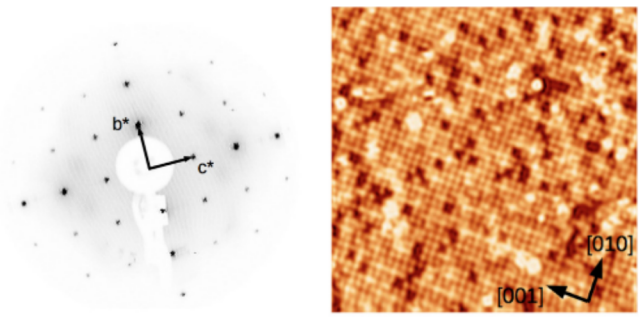

FIG. 22. (a) LEED pattern at 40 eV of the Al_5Co_2(100) surface prepared at 1043 K and (b) 30×30 nm^2 STM image ($V_b = -2$ V; $I_t = 0.08$ nA).

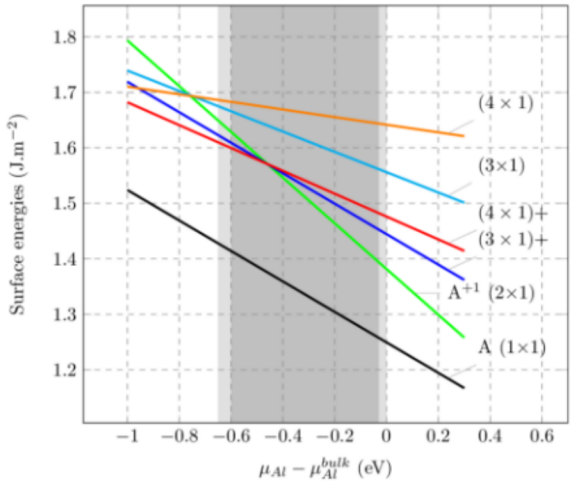

FIG. 23. Calculated surface energies for the different models matching the (100) surface prepared at different temperatures, plotted as a function of $\mu_{Al} - \mu_{Al}^{bulk}$.

IV. DISCUSSION

A. Influence of the preparation conditions

The structures of the three low-index (100), (001), and ($2\bar{1}0$) surfaces are found to depend on the annealing temperature used during surface preparation, leading to several surface reconstructions. For the (001) surface [3], the structure evolves from a (2×2) reconstruction at low temperature (823 K) to a denser $(\sqrt{3} \times \sqrt{3})$R30° structure at 973 K (model $P_{6\,Al\,miss}^{(\sqrt{3}\times\sqrt{3})R30^\circ}$ [3]) and finally to a (1×1) structure at higher annealing temperature (1043 K). For the (100) surface, a mixture of (2×1), (3×1), and (4×1) reconstructions is observed at low temperature (823 K). The structure evolves with increasing temperature to a surface exhibiting only a (2×1) reconstruction, corresponding to what might be the A^{+1} or A^{-1} models. This evolution cannot be explained by simply comparing atomic densities for the different models and is not perfectly understood yet. At even higher temperature, the structure evolves toward a bulk terminated surface with A termination. The calculations of the corresponding surface energies (Fig. 23) confirm this behavior in the Al-rich part, since the most stable surface structures correspond to the ones observed at higher temperature.

Contrary to the (001) and (100) low-index surfaces, the structure of the ($2\bar{1}0$) does not depend much on the annealing temperature. In this case, the surface preparation conditions have an influence on the value of the chemical potential. Here, the most stable surface model (P_B or P_{B-4Co}), among the ones considered here, depends on the value of the Al chemical potential.

B. Impact of bulk structure on surfaces

Figure 24 shows a side-view of the structural models built for the three Al_5Co_2 low-index surfaces. In all cases, the observed terminations intersect covalently bonded motifs. In the following, we discuss the interplay between the two-dimensional surface and the three-dimensional cluster structure.

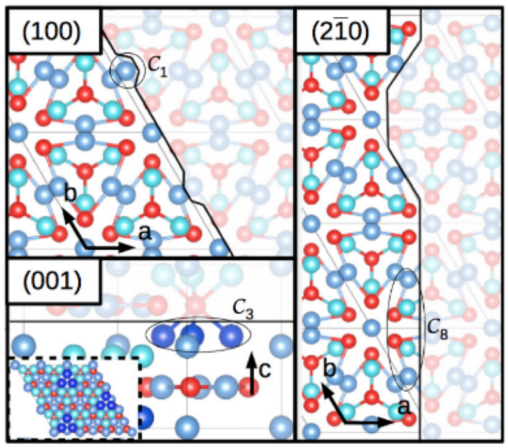

FIG. 24. Side view of terminations for the different surfaces studied. Terminations intersect covalently bonded motifs, leaving groups of atoms at their surfaces [a group of one atom C_1 for the A^{+1} model (100), a group of three atoms C_3 for the $P_{6\,Al\,miss}^{(\sqrt{3}\times\sqrt{3})R30^\circ}$ model (001), and a group of eight atoms C_8 for the P_B model (2$\bar{1}$0)]. Inset is showing a top view of the (001) surface, highlighting the triangular shaped ensembles forming a $(\sqrt{3}\times\sqrt{3})R30^\circ$ reconstruction.

For the (100) surface (A^{+1} model), the termination intersects covalently bonded motifs, leaving a group C_1 of only one atom lying at the surface. It is the protruding atom in Fig. 24. This atom is involved in the planar motif $(Co_2)_3(Al_2)_3$. The formation of the surface then requires to break at least two covalentlike bonds, which corresponds to an energy equal to -0.80 eV (2×-0.40 eV). Here, we have considered the A^{+1} model as surface termination but a similar conclusion is reached in the case of the A^{-1} model. At higher temperature, the surface corresponds to the complete (1×1) A termination for which the cluster integrity is totally preserved, in agreement with surface energy calculations.

The (001) surface terminates at specific planes perpendicular to the [001] direction (pure Al planes) and shows a $(\sqrt{3}\times\sqrt{3})R30^\circ$ reconstruction. This corresponds to the removal of 2/3 of the surface Al_3 groups belonging to the three-dimensional $(Co_1)(Al_3)_6$ clusters. The presence of these triangular shaped atomic ensembles (labeled C_3) at the surface, requires to break at least three strong Al-Co covalentlike bonds ($3\times-0.49=-1.47$ eV). In addition, C_3 is weakly bonded to the underlying substructure.

These results are in agreement with the behavior observed experimentally where C_3 is desorbing at higher temperature, which is similar to the one observed for the (100) surface. For the (2$\bar{1}$0) surface, the termination intersects covalently bonded motifs leaving at the surface a group C_8 of eight atoms, involving both the three-dimensional $(Co_1)(Al_3)_6$ cluster and the planar $(Co_2)_3(Al_2)_3$ motif. The presence of C_8 at the surface requires to break eight Al-Co covalentlike bonds within the 3D cluster and the 2D motif, which correspond to an energy roughly equal to -3.5 eV. Here, C_8 is quite strongly linked with the subsurface and the surrounding, since the energy of covalentlike Al-Co bonds involved to maintain C_8 at the surface is roughly equal to -3.7 eV. This result might partially explain the specific reconstruction observed, even at 1043 K. However, further study considering all interatomic interactions leads to a different interpretation, since the interatomic interactions of C_8 with the subsurface and the surrounding atoms are quite weak.

In the same way, for the (2$\bar{1}$0) surface, we would expect that P_A, P_{A-4Co}, and P_C are not so stable, since they involve either isolated Co atoms at the surface, without their pentagonal environment (P_A, P_{A-4Co}), or isolated pentagonal aluminum rings, without any central cobalt atom (P_C). At first sight, the structural models P_B and P_D are not so different, since they both involve lines of pentagonal $CoAl_5$ motifs. However, the strong covalentlike Al-Co bonds involved in these two structures are quite different. In P_D-type models, the number of broken bonds is more than twice compared to the P_B model.

We conclude that a first-neighbor bonding strength study highlights (i) the interplay of the three-dimensional cluster structure with the two-dimensional surface, and (ii) the influence of the annealing temperature on the surface terminations. However, it is insufficient to get by itself a detailed picture and to predict the surface structure at different temperatures.

C. (001), (100), and (2$\bar{1}$0) surfaces: a comparison

Surface energies of the different models found for the three surfaces are plotted in Fig. 25. For the Al-rich part, the most stable surface termination corresponds to P_{B-4Co}, while it is P_B for the Co-rich part. For intermediate values of μ_{Al}, models for (100) and (001) [3] surfaces show lower surface energies. The surface composition and the surface atomic density have been shown to have a strong impact on the surface stability [25]. The calculated atomic densities of the three surfaces are similar and take values of 72 atoms/nm^3 in the first 4 Å of the surface selvedge for the P_B model of the (2$\bar{1}$0) surface, 66 atoms/nm^3 for the (100) surface, and 80 atoms/nm^3 for the (001) surface. Interestingly, it appears for the Al-rich part that surface energies are proportional to the number of Co atoms in the first 4 Å of the respective surfaces selvedge. The more Co atoms are absent, the lower the surface energies are. This is somehow not too surprising as pure Al surfaces

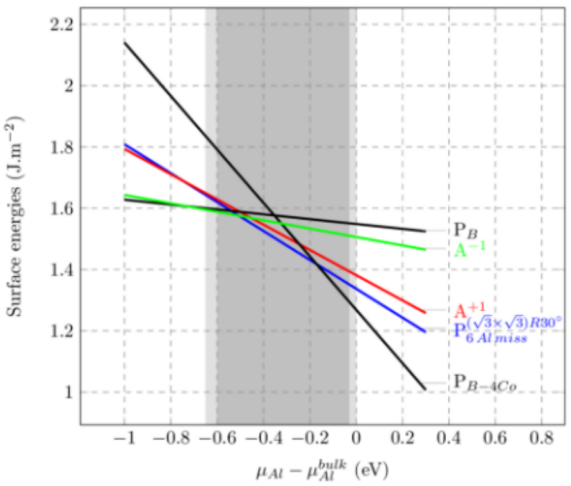

FIG. 25. Calculated surface energies for the best models for all different surfaces studied, plotted as a function of $\mu_{Al}-\mu_{Al}^{bulk}$.

have lower surface energies than Co surfaces (i.e., Al(111) 1.199 J m^{-2}, Al(100) 1.347 J m^{-2}, Co(0001) 2.775 J m^{-2}, Co($10\bar{1}0$)a 3.035 J m^{-2} [26]). The anisotropy of the calculated surface energies is relatively small, hence a homogeneous mixture of all three surfaces is expected when preparing the Al_5Co_2 intermetallic for catalytic purposes.

V. SUMMARY AND CONCLUSIONS

$Al_5Co_2(2\bar{1}0)$ and (100) surfaces have been studied using experimental and computational methods. After annealing the sample at 973 K, the $(2\bar{1}0)$ surface shows a (2×1) reconstruction with 12-Å-wide lines parallel to the [001] direction. Among the different models tested, one termination with two different variations (P_B and P_{B-4Co}) geometrically matches the experimental data. The P_B and P_{B-4Co} models are almost identical and differ by the presence/absence of four surface Co atoms. The (100) surface is also showing a (2×1) reconstruction and is built of narrower lines also in the [001] direction.

Among the considered models, model A^{+1} shows the lowest surface energy for the largest range of the chemical potential considered. Simulated STM images suggest that model A^{-1}, showing lesser bias dependency, matches the experimentally observed surface.

These surface structures can be interpreted as truncated motif parts (an intersection of covalentlike bonded cluster/motif) forming the lines of the observed reconstructions. In the case of the (100) surface, these truncated parts are desorbing if considering the A^{+1} or some Al atoms segregate to the surface for the A^{-1} model, so that at higher temperature, the observed (1×1) terminated surface can be observed (A termination). A similar behavior was observed for the (001) surface [3]. The $(2\bar{1}0)$ surface is mostly unchanged at higher temperatures although faceting can be observed.

Because it has a high number of surface Co atoms, the $(2\bar{1}0)$ surface is considered as the most interesting candidate for the heterogeneous semihydrogenation of acetylene. Depending on the Co atom content within the topmost surface layer, the reactivity of the surface is expected to vary. However, it is likely that under reaction conditions both chemical variants (P_B and P_{B-4Co}) will be present at the $(2\bar{1}0)$ surface of this intermetallic.

A perspective of this work would be to calculate the adsorption energies and the adsorption sites for hydrogen and other involved molecules for the different models. Nudged elastic band (NEB) calculations could be used to determine the reaction path especially on the promising $(2\bar{1}0)$ surface models. Reactivity properties could be further investigated experimentally by *in situ* XPS measurements.

ACKNOWLEDGMENTS

This work was supported by the ANR CAPRICE 2011-INTB 1001-01, the European C-MAC consortium and COST Action CM0904 "Intermetallic compounds as catalyst for steam reforming of methanol (IMC-SRM)," the CNRS (project PICS-INCAS-05892). M.M. also acknowledges financial support from the "Région Lorraine" during his PhD. This work was granted access to the HPC resources of GENCI-IDRIS under the allocation 2015096339.

[1] *Complex Metallic Alloys: Fundamentals and Applications*, edited by J.-M. Dubois and E. Belin-Ferré (Wiley-VCH, Weinheim, 2011).
[2] K. Kovnir *et al.*, Sci. Tech. Adv. Mater. **8**, 420 (2007).
[3] M. Meier, J. Ledieu, M.-C. De Weerd, Ying-Tzu Huang, G. J. P. Abreu, K. Pussi, R. D. Diehl, T. Mazet, V. Fournée, and É. Gaudry, Phys. Rev. B **91**, 085414 (2015).
[4] S. Song and E. R. Ryba, Philos. Mag. Lett. **65**, 85 (1992).
[5] A. Gwyer, Z. Anorg. Allg. Chem. **57**, 113 (1908).
[6] A. J. Bradley and G. C. Seager, J. Inst. Met. **64**, 81 (1937).
[7] U. Burkhardt, M. Ellner, Yu. Grin, and B. Baumgartner, Powder Diffr. **13**, 159 (1998).
[8] K. W. Richter and D. T. Gutiérrez, Intermetallics **13**, 848 (2005).
[9] A. Ormeci and Y. Grin, Isr. J. Chem. **51**, 1349 (2011).
[10] S. A. Villaseca, J. M. Dubois, and É. Gaudry, Philos. Mag. **91**, 2894 (2011).
[11] G. Kresse and J. Hafner, Phys. Rev. B **47**, 558 (1993).
[12] G. Kresse and J. Hafner, Phys. Rev. B **49**, 14251 (1994).
[13] G. Kresse and J. Furthmüller, J. Comput. Mater. Sci. **6**, 15 (1996).
[14] G. Kresse and J. Furthmüller, Phys. Rev. B **54**, 11169 (1996).
[15] P. E. Blochl, Phys. Rev. B **50**, 17953 (1994).
[16] G. Kresse and D. Joubert, Phys. Rev. B **59**, 1758 (1999).
[17] J. P. Perdew, K. Burke, and M. Ernzerhof, Phys. Rev. Lett. **77**, 3865 (1996).
[18] J. P. Perdew, K. Burke, and M. Ernzerhof, Phys. Rev. Lett. **78**, 1396 (1997).
[19] K. Momma and F. Izumi, J. Appl. Crystallogr. **44**, 1272 (2011).
[20] J. L. F. Da Silva, Phys. Rev. B **71**, 195416 (2005).
[21] J. Tersoff and D. R. Hamann, Phys. Rev. Lett. **50**, 1998 (1983).
[22] J. Tersoff and D. R. Hamann, Phys. Rev. B **31**, 805 (1985).
[23] J. K. Nørskov, F. Studt, F. Abild-Pedersen, and T. Bligaard, *Fundamental Concepts in Heterogeneous Catalysis* (Wiley, New Jersey, 2014).
[24] H. Ohtani, *Al-Co Phase Diagram*, ASM Alloy Phase Diagrams Database, P. Villars, editor-in-chief; H. Okamoto and K. Cenzual, section editors; http://www1.asminternational.org/AsmEnterprise/APD (ASM International, Materials Park, OH, 2006).
[25] B. Unal, C. J. Jenks, and P. A. Thiel, Phys. Rev. B **77**, 195419 (2008).
[26] L. Vitos, A. Ruban, H. Skriver, and J. Kollár, Surf. Sci. **411**, 186 (1998).